Structural Complexity in Metal−Organic Frameworks: Simultaneous Modification of Open Metal Sites and Hierarchical Porosity by Systematic Doping with Defective Linkers

Zhenlan Fang,[†] Johannes P. Dürholt,[†] Max Kauer,[‡] Wenhua Zhang,[†] Charles Lochenie,[∥] Bettina Jee,[⊥] Bauke Albada,[§] Nils Metzler-Nolte,[§] Andreas Pöppl,[⊥] Birgit Weber,[∥] Martin Muhler,[‡] Yuemin Wang,*,[‡] Rochus Schmid,*,[†] and Roland A. Fischer*,[†]

[†]Inorganic Chemistry II—Organometallics & Material Chemistry, [‡]Physical Chemistry I and Laboratory of Industrial Chemistry, and [§]Inorganic Chemistry I—Bioinorganic Chemistry, Ruhr-University, Universitätsstrasse 150, 44801 Bochum, Germany
[∥]Anorganische Chemie II, Universität Bayreuth, Universitätsstrasse 30, NW I, 95440 Bayreuth, Germany
[⊥]Institute of Experimental Physics II, University of Leipzig, Ritterstrasse 26, 04109 Leipzig, Germany

S *Supporting Information*

ABSTRACT: A series of defect-engineered metal−organic frameworks (DEMOFs) derived from parent microporous MOFs was obtained by systematic doping with defective linkers during synthesis, leading to the simultaneous and controllable modification of coordinatively unsaturated metal sites (CUS) and introduction of functionalized mesopores. These materials were investigated via temperature-dependent adsorption/desorption of CO monitored by FTIR spectroscopy under ultra-high-vacuum conditions. Accurate structural models for the generated point defects at CUS were deduced

by matching experimental data with theoretical simulation. The results reveal multivariate diversity of electronic and steric properties at CUS, demonstrating the MOF defect structure modulation at two length scales in a single step to overcome restricted active site specificity and confined coordination space at CUS. Moreover, the DEMOFs exhibit promising modified physical properties, including band gap, magnetism, and porosity, with hierarchical micro/mesopore structures correlated with the nature and the degree of defective linker incorporation into the framework.
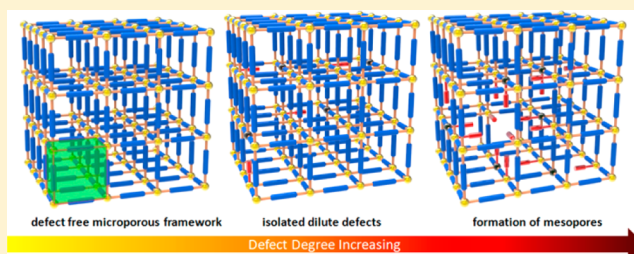
1. INTRODUCTION

Defects of various natures and length scales are well-established key attributes of crystalline condensed matter, and understanding a material's defect structure offers control over its performance.[1,2] In contrast, the properties of metal−organic frameworks (MOFs), a fascinating class of organic/inorganic materials, are mainly conceived from coordination network topology, implying both long-range and local structural perfection.[3−15] Some MOFs exhibit coordinatively unsaturated sites (CUS) at the metal ion nodes of the framework, and this local structural feature mediates adsorption, transport, and reactive phenomena in analogy to active sites at the surface of typical heterogeneous catalysts.[16−25] However, the restricted specificity and the confined coordination space of native CUS are significant limitations.

Only recently it has become evident that defect-engineering may be a powerful strategy going beyond the drawbacks of the parent MOF system. A few groups have started out investigating structural disorder in the crystal lattice of MOFs[26−31] or correlated defects with functions such as catalysis[32−35] and gas absorptions.[36−39] Several approaches were proposed to introduce defects in MOFs: (a) acid

modulators have been used in the synthesis of missing-linker MOFs such as HKUST-1[39] and UiO-66;[34,37] (b) the postsynthetic treatment of MOFs with inorganic acids leads to the generation of MIL-100(Fe) with missing linkers;[35] (c) fast precipitation can also result in the formation of missing-linker defective MOFs;[36] (d) the mixed-linker approach including a metal−ligand−fragment coassembly strategy has been adopted to synthesize defective MOFs.[27,31−33,36,38] These studies primarily focus on the synthesis and application of MOFs with defects; however, a detailed molecular-level understanding of electronic and steric properties at the defective CUS, as well as the relationship between the defect sites and corresponding properties, presents a major challenge. Such comprehensive and fundamental understanding of the structural defects is a key step for a rational design of defect-engineered MOFs (DEMOFs). It requires the combination of analytical techniques suited to probe the local environment and state of the art quantum chemical theory and molecular
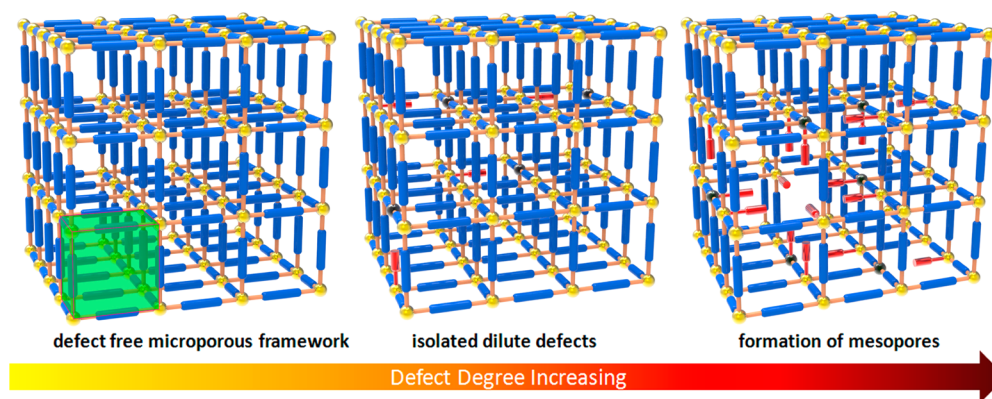
Figure 1. Defect-engineered MOFs (DEMOFs). The modulation of the defect structure on the micro- and mesoscales by defective linker doping of the framework is shown. The blue and short red sticks represent perfect and defective linkers. The yellow and black balls represent perfect and defective metal sites, respectively. The green highlighted unit indicates parent micropores.

modeling of MOFs to properly interpret the experimental evidence.

In this work, we selected $[Cu_3(btc)_2]$ (btc^{3-} = 1,3,5-benzenetricarboxylate),[40] also called HKUST-1 (MOF-199), as the candidate of choice for our investigations on DEMOFs. A series of defective HKUST-1 samples were obtained by controlled framework incorporation of defective linkers during synthesis and crystal growth. We employed carbon monoxide (CO) as a probe molecule for characterization of the modified CUS and studied low-temperature CO adsorption and desorption by sophisticated ultra-high-vacuum Fourier transform infrared spectroscopy (UHV-FTIRS).[41,42] The high-quality IR data in conjunction with accurate density functional theory (DFT) calculations allow us to gain detailed insight into the structural and electronic properties of DEMOFs which are significantly modified with respect to the parent MOFs by systematic and controlled defective linker doping. Interestingly, we found thus implemented small- and large-scale defects to be correlated to each other. Both aspects are controlled by the nature of the defective linkers integrated into the framework through substitution of variable fractions of the parent organic linkers without affecting the network topology. Our DEMOFs described herein provide diverse modified CUS with multivariate electronic and steric properties. The coordination modulating effect of defective linkers and anion of copper salts combined by the cluster of local and small-scale point defects finally results in the emerging mesoporosity of the material, which offers the added value of a large-scale defect structure (Figure 1).

2. EXPERIMENTAL SECTION

2.1. Sample Preparation. Either $Cu(NO_3)_2 \cdot 3H_2O$ or $Cu(BF_4)_2 \cdot 6H_2O$ (1.614 mmol) was dissolved in 6 mL of distilled water, and samples of Lx (n mmol) and H_3btc (1.076 − n mmol) were dissolved in a 12 mL mixture of anhydrous N,N-dimethylformamide and ethanol with a volume ratio of 1:1 (for D1−D3). For D4, however, samples of $Cu(NO_3)_2 \cdot 3H_2O$ (0.538 mmol) and the mixture of H_3btc (0.359 − n/3 mmol) and L4 (n/3 mmol) were dissolved in 9 mL of anhydrous ethanol, respectively. Then the two clear solutions were combined in a sealed bottle (25 mL), stirred for 20 min, and then heated at 70 °C for 12 h, followed by cooling to room temperature. The obtained turquoise microcrystalline powders were filtered off, washed thoroughly with ethanol, acetone, and dichloromethane, respectively, to remove residual precursor species, and then dried in air for a few hours. The samples were activated for 24 h (~10^{-3} mbar, D1−D3 at

215 °C, D4 at 170 °C) and stored under argon. The full set of samples and the numbering scheme are given in the Supporting Information.

2.2. Infrared Spectroscopy. UHV-FTIRS experiments were performed using a special apparatus described elsewhere.[42−44] The optical path inside the IR spectrometer and the space between the UHV chamber and the spectrometer were evacuated, resulting in a superior sensitivity and stability of the system. The samples were pressed into a gold-plated stainless steel grid (previously cleaned by heating to 850 K) and activated in the UHV chamber at 450 K. Prior to each exposure, a spectrum of clean samples was used as a background reference. All UHV-FTIR spectra were collected with 512 scans at a resolution of 4 cm^{-1} in transmission mode.

2.3. Computational Methods. The structures were optimized by a quantum mechanics/molecular mechanics (QM/MM) method for a single defect, mechanically embedded in a perfect $[Cu_2btc_3]$ environment, using periodic boundary conditions for the MM system. The QM-parametrized MOF-FF force field[45] was used to describe the surrounding MOF. The QM region consists of the defect paddlewheel and the adjacent aromatic system (phenyl or pyridyl), replacing a C−C bond by a C−H bond in the QM system. A hydrogen link atom saturates the QM system (see the Supporting Information for further details). The same dispersion-corrected hybrid density functional theory level (B3LYP/cc-pVDZ+D3) as used in the reference calculation for the MOF-FF parametrization was utilized in the QM part. The program packages pydlpoly[45] and TURBOMOLE 6.3 were used to implement the QM/MM coupling. The normal modes were computed via analytic second derivatives for the QM system in the QM/MM-optimized structure. The CO stretching mode frequencies were scaled to reproduce the experimental value for free CO in the gas phase on the given level of theory.

2.4. Further Characterization Data. Full details on the analytical, spectroscopic, and other important characterization methods and respective data are given in the Supporting Information, including the following: elemental analysis (EA), X-ray powder diffraction (PXRD), thermogravimetry (TG), differential scanning calorimetry (DSC), Brunauer−Emmett−Teller (BET) analysis, pore size distributions, routine FTIR, ^1H NMR, high-performance liquid chromatography (HPLC) of quantitatively digested samples, UV−vis, diffuse reflectance spectroscoy (DRS), magnetic susceptibility, electron paramagnetic resonance (EPR), and high-resolution X-ray photoelectron spectroscopy (XPS).

3. RESULTS AND DISCUSSION

3.1. Defective Linker Doping: Synthesis and Composition. $[Cu_3(btc)_2]$ holds promise for introducing defective CUS by the mixed-component approach.[33] Some examples of mesostructured variants were also reported and are known to be thermally robust.[39,46,47] In this work, we systematically incorporate a set of defective linkers into the parent framework

Scheme 1. Defective Linker Concept for DEMOFs^a
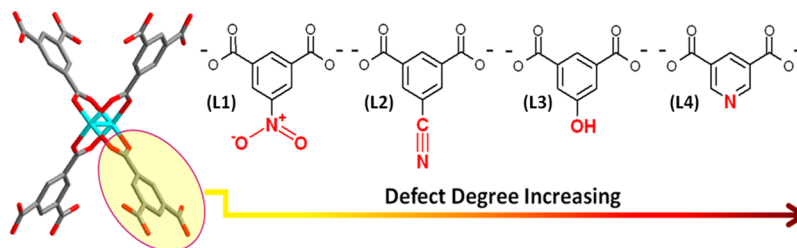
^{a}Illustration of increasing defect degree by Lx^{2-} incorporation, i.e., btc^{3-}/Lx^{2-} exchange. The defective linkers L1−L3 were chosen as benzene-1,3-dicarboxylates with various functional groups at the 5-position (L1 = nidc^{2-}, −NO$_2$; L2 = cydc^{2-}, −CN; L3 = hydc^{2-}, −OH), and L4 was pyridine-3,5-dicarboxylate (pydc^{2-}). The drawing shows only the Cu−Cu paddlewheel unit and highlights the changed btc^{3-} linker (color code of the atoms: Cu, turquoise; C, gray; O, red; N, blue). Other structural features are omitted for clarity.
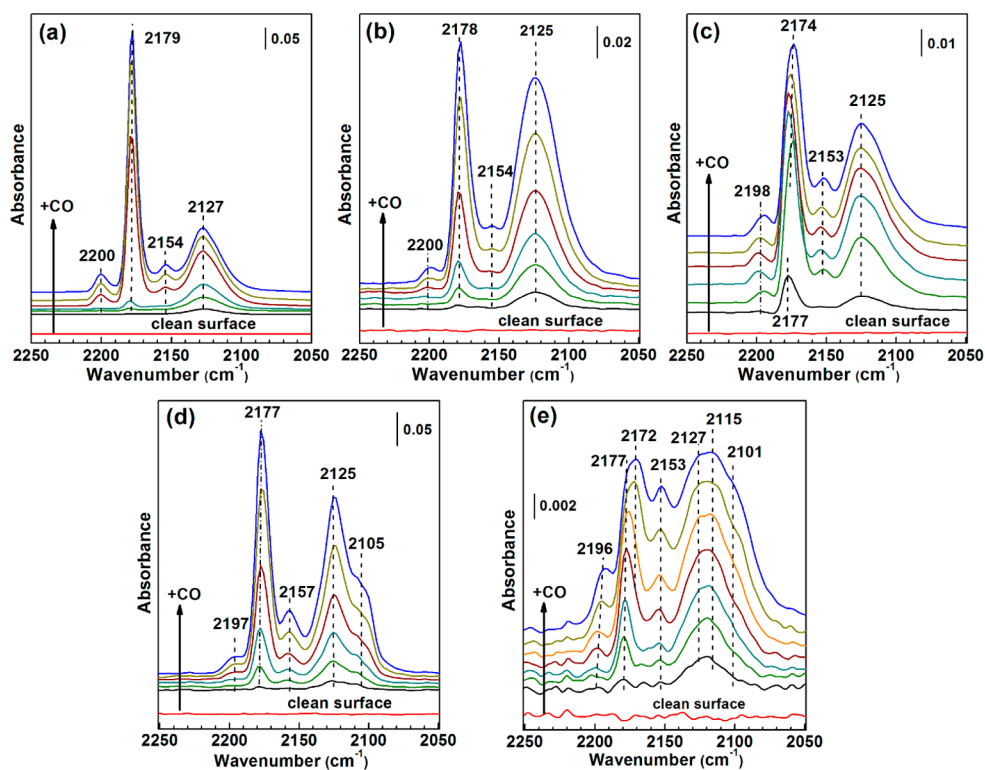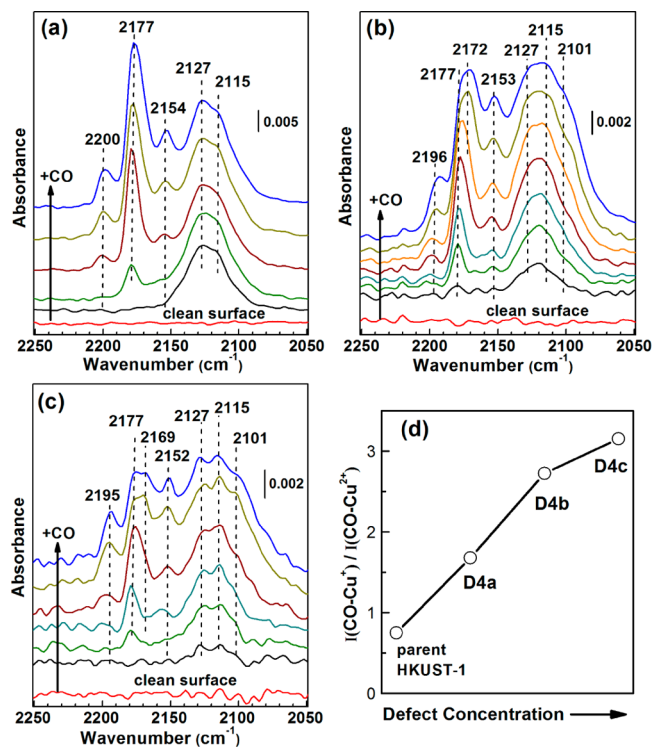

Figure 2. Experimental confirmation of modified copper sites by varying the defective linkers. UHV-FTIR spectra were obtained after representative DEMOF samples D1−D4 with different defective linkers L1−L4 were exposed to various amounts of CO from 1×10^{-6} mbar (black line) to 3×10^{-4} mbar (blue line) at 90 K. Prior to exposure, each sample was heated to 450 K to remove all adsorbed species. Clean (activated) DEMOF samples exhibit the general formula $[Cu_3(btc)_{2-d}(Lx)_d]$ (D1−D4): (a) $[Cu_3(btc)_2]$ (parent); (b) $[Cu_3(btc)_{1.67}(L1)_{0.33}]$ (D1e); (c) $[Cu_3(btc)_{1.63}(L2)_{0.37}]$ (D2d); (d) $[Cu_3(btc)_{1.60}(L3)_{0.40}]$ (D3e); (e) $[Cu_3(btc)_{1.71}(L4)_{0.29}]$ (D4b). See the Supporting Information for the full set of samples and further characterization and analytical data.

(L1 = 5-nitroisophthalate (nidc^{2-}), L2 = 5-cyanoisophthalate (cydc^{2-}), L3 = 5-hydroxyisophthalate (hydc^{2-}), L4 = pyridine-3,5-dicarboxylate (pydc^{2-}); see Scheme 1). Our approach is different from the aforementioned methods a−d mainly focusing on missing-linker defects,[34,35,37,39] or defects resulting from substitution of ligands with significantly different structures.[32,36,38] Herein, Lx (x = 1−4) have structures and coordination chemistries very similar to those of the parent linker, i.e., btc^{3-}, and only one carboxylate ligator site is replaced by weaker interacting ligators. This systematic doping with defective linkers can offer the opportunity not only to finely tune the engineered defects on CUS but also to modify the MOFs' porosity due to defect clustering and the coordination modulation by defective linkers during synthesis

and crystal growth.[38] In the parent, "perfect" form, $[Cu_3(btc)_2]$ exhibits two Cu^{2+} sites as the native CUS at the axial positions of the Cu$_2$(O$_2$CR)$_4$ paddlewheel nodes of the framework. We obtained the series of DEMOFs (Dx) of formula $[Cu_3(btc)_{2-d}(Lx)_d]$ (x = 1−4) listed in Table S1 of the Supporting Information, in which the defects result from framework incorporation of defined amounts (d) of defective linkers Lx. Notably, in the case of unchanged Cu^{2+} oxidation states for D1−D4, some anions A (NO$_3^-$, BF$_4^-$) stemming from the applied copper salts CuA$_2$ for synthesis must be present for charge compensation of the missing carboxylate of L1−L4 with respect to trivalent btc^{3-}. All materials were characterized by EA, TG, DSC, N$_2$ gas adsorption/desorption, routine FTIR, UV−vis, DRS, ^{1}H NMR, and HPLC of

quantitatively digested samples. The PXRD peaks of all samples are indexed and match with the pattern of parent $[Cu_3btc_2]$ (see Figure S1 in the Supporting Information). The combined data confirm the phase purity and sample composition, substantiate framework incorporation of Lx, rule out the presence of physisorbed btc^{3-} or Lx, and in addition preclude the presence of any significant amounts of anions A. Accordingly, the empirical formulas $[Cu_3(btc)_{2-d}(Lx)_d]$ and structural assignments for D1–D4 are justified (see Table S1 in the Supporting Information for details). We thus anticipate the generation of modified CUS compared to the parent $[Cu_3btc_2]$ as a consequence of the Lx doping leading to mixed-valence Cu^{1+}/Cu^{2+} defects by a reduction from one of the redox-active species in the growth solution (i.e., ethanol).

3.2. Probing Local Defects by UHV-FTIR Spectroscopy and DFT Modeling.

Representative samples were selected for characterization of CUS by CO adsorption and in situ UHV-FTIRS at 90 K. The corresponding IR spectra for different DEMOF samples prepared by varying the defective linkers Lx (L1–L4) with comparable doping levels (15–20%) or by increasing the concentration of L4 (pydc^{2-}) are presented in Figures 2 and 3, respectively. The expected bands between 2179 and 2174 cm^{-1} stem from CO molecules bound to native Cu^{2+} CUS through electrostatic and σ-donation interactions similar to those of the parent $[Cu_3btc_2]$.[41] However, samples

D1–D4 exhibit an intense and broad second C–O stretching region ranging from 2130 to 2100 cm^{-1}, which turned out to be highly sensitive to the nature (Figure 2) and doping level (Figure 3) of Lx. The pronounced red-shifted IR bands suggest a variety of CO species adsorbed at electronically modified, i.e., reduced, copper sites due to the enhanced π back-donation.[48] The assumption of Cu^{1+} formation (defective Cu^{1+}/Cu^{2+} pairs) is consistent with the absence of anions A and is confirmed by XPS results (see Figures S11–S15 in the Supporting Information for details). In addition, the generation of reduced Cu^{1+} CUS by defective linker incorporation agrees with the shift of the band gap to higher energies (diffuse reflectance spectra, Figure 8) and the results of the magnetic measurements (Figure 9). The framework is redox responsive, and thus, it compensates for the missing carboxylate by Cu^{1+} formation.[49,50] A quantitative analysis of the integrated intensity ratio of the Cu^{1+}-related to the Cu^{2+}-related CO bands (Figure 3d) reveals that the abundance of Cu^{1+} CUS in D4 is gradually increased with increasing degree of L4 incorporation. It should be noted that the extinction coefficient of CO–Cu^{1+} is generally more than 1 order of magnitude higher than that of CO–Cu^{2+},[48,51] indicating a very low abundance of Cu^{1+} (native) defects in the parent HKUST-1 (a few percent).

To corroborate this reasoning and to gain deeper insight into the nature of the generated defects at the copper paddlewheel moieties, QM/MM calculations of isolated defects were performed. The key strategy of the calculations is that a sufficiently large QM part (dispersion-corrected hybrid DFT level) is mechanically embedded into a (periodic) MM model using the QM-derived MOF-FF force field[45] to maintain the defective linkers in the proper structure. Full details about the theoretical methods and results are given in the Supporting Information. The calculations focused on D4 with the largest deviation from the parent structure and D1 with the smallest deviation as inferred from the UHV-IR experiments (Figures 2 and 3). Different binding modes of CO at the CUS have been considered, but only for η^1 C-coordinated CO stable minima could be optimized, for which vibrational normal modes (for the QM subsystem) have been computed in turn (Figure 4; Figure S17, Supporting Information). First, an assignment of the experimentally observed CO bands to a nonreduced Cu^{2+}/Cu^{2+} defect can safely be ruled out by the calculations, corroborating the experimental results. On the other hand, the matching of the calculations with the UHV-IR spectra is in favor of the reduced Cu^{1+}/Cu^{2+} defect. Importantly, a theoretical estimate of the relative redox potentials (using a continuum solvation model) indicates that the cationic Cu^{2+}/Cu^{2+} defect is much more prone to reduction as compared to the native Cu^{2+}/Cu^{2+} paddlewheel (see the Supporting Information). The additional unpaired electron delocalizes over both copper sites with a symmetric charge distribution for the CO-free defective Cu^{1+}/Cu^{2+} paddlewheel unit (Table S6, Supporting Information). This is supported by the XPS data, which show that the Cu^{1+} and Cu^{2+} ions in the Cu^{1+}/Cu^{2+} dimer cannot be distinguished (Figure S12, Supporting Information).

Upon coordination of the first CO (Figure 4a), the additional electron is localized to generate a Cu^{1+} site binding one CO with strong π back-donation. The calculated frequency of 2097 cm^{-1} together with the relatively high binding energy of 28.1 kcal/mol for the (CO)Cu^{1+} species generally explains the red-shifted CO bands around 2120 cm^{-1} of the spectra (Figures 2 and 3). Coordination of the second CO at the
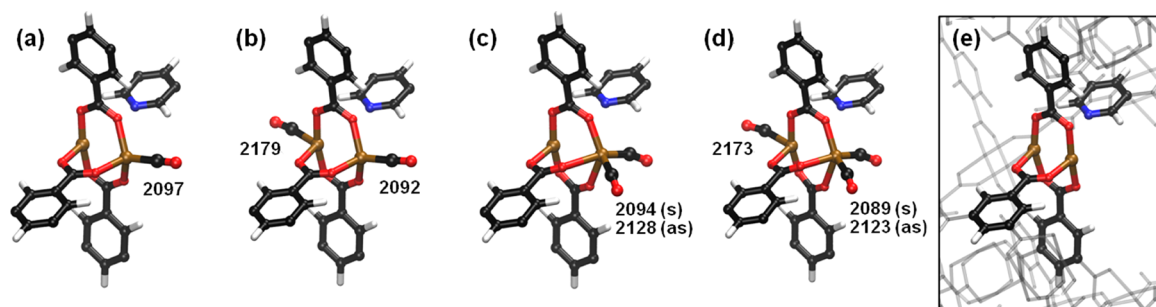

Figure 3. Experimental confirmation of modified copper sites by varying the concentration of the incorporated defective linker L4. UHV-FTIR spectra were obtained after $[Cu_3(btc)_{2-d}(pydc)_d]$ (D4) was exposed to various amounts of CO from 1×10^{-6} mbar (black line) to 3×10^{-4} mbar (blue line) at 90 K. Prior to exposure, each sample was heated to 450 K to remove all adsorbed species. The concentration (d) of the defective linker L4 (pydc^{2-}) was varied: (a) $[Cu_3(btc)_{1.90}(L4)_{0.10}]$ (D4a); (b) $[Cu_3(btc)_{1.71}(L4)_{0.29}]$ (D4b); (c) $[Cu_3(btc)_{1.41}(L4)_{0.59}]$ (D4c). (d) Integrated intensity ratio of IR bands, i.e., Cu^{1+}-related (2101, 2115, and 2127 cm^{-1}) to Cu^{2+}-related (2169 and 2177 cm^{-1}), as a function of the defect concentration.

Figure 4. QM/MM-computed binding modes of CO. (a−d) The QM/MM model for a local mixed-valence defect $Cu^{1+}/Cu^{2+}(btc)_3(pydc)$ typical for sample D4 is shown, and energetically feasible binding modes for one to three coordinated (adsorbed) CO molecules are given (only the QM system for clarity; Cu, brown; C, black; O, red; N, blue; H, white) together with the computed (scaled) CO stretching normal-mode frequencies (cm^{-1}). (e) For comparison the defect is shown in a close-up, indicating the embedding of the QM system in the MM environment.
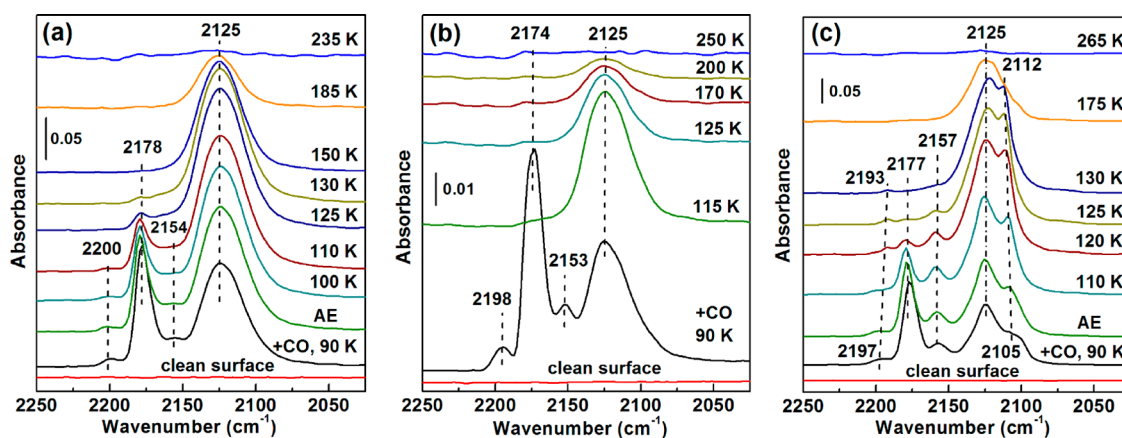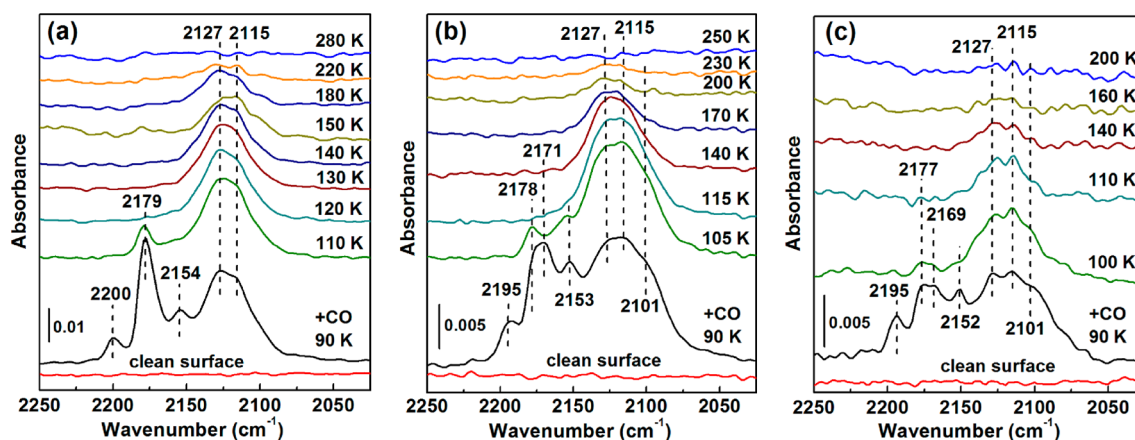

Figure 5. Thermal stability of CO adsorbed on defective sites by varying the defective linkers Lx. UHV-FTIR spectra were obtained after CO (1×10^{-4} mbar) adsorption on clean DEMOF samples at 90 K and then heating to the indicated temperatures. The defective linkers Lx (L1 = nidc$^{2−}$, L2 = cydc$^{2−}$, L3 = hydc$^{2−}$) in DEMOFs were varied: (a) $[Cu_3(btc)_{1.67}(L1)_{0.33}]$ (D1e); (b) $[Cu_3(btc)_{1.63}(L2)_{0.37}]$ (D2d); (c) $[Cu_3(btc)_{1.60}(L3)_{0.40}]$ (D3e).

remaining Cu^{2+} site (Figure 4b) exhibits a lower binding energy of 9.6 kcal/mol, with the corresponding $\nu(CO)$ mode (2179 cm^{-1}) falling in the same range as that of nondefect Cu^{2+}/Cu^{2+} paddlewheels, which are also present in the samples. The alternative, simultaneous coordination of the first and second CO molecules at the same Cu^{1+} site (Figure 4c), keeping the Cu^{2+} site vacant, is ∼6.5 kcal/mol less stable; consequently, such a situation is unlikely in the real samples. Most significantly, the calculated results indicate that a third CO molecule may weakly bind (2 kcal/mol) to the electron-rich Cu^{1+} site if the Cu^{2+} site is already occupied (Figure 4d). The frequency of the resulting asymmetric CO stretch mode of this geminal $(CO)_2Cu^{1+}$ species calculated to be 2123 cm^{-1} corresponds to the characteristic feature around 2150 cm^{-1} in the UHV-IR spectra. Due to the weak binding, it will be the least populated and is the first thermally removed (see Figures 5 and 6 and the discussion below). This third CO coordination results from the more open coordination space at the defective CUS. Such species could not be found for the parent $[Cu_3btc_2]$ by our DFT calculations.[41] Interestingly, a similar stable minimum could not be located in the case of D1 as the steric situation of L1 (5-nitrobenzene-1,3-dicarboxylate, nidc$^{2−}$) is much closer to that of btc$^{3−}$ than that of L4 (pydc$^{2−}$; see Table S6, Supporting Information). This is in accord with the experimental observation that the feature around 2150 cm^{-1} for D1 is nearly invisible (Figure 2b).

The data derived from modeling of D1 and D4 are used to assign the $\nu(CO)$ bands for D2 and D3. Noticeably, the molecular models considered in this study could not explain the blue-shifted band around 2200 cm^{-1} in the experimental spectra. It may be related to minority CO bound to other types of defect sites probably located at the external crystallite surface or at cracks inside the crystallites.[41] These theoretical results are used to extrapolate to the real systems, which is particularly valid for a lower framework-incorporated Lx concentration (d = ∼5%), e.g., D4a (Figure 3a). For higher concentrations ($d >$ 20%) the influence of nearest neighbor defects is likely to become more important, leading to an increasing diversity of environments for different species, and thus, the spectroscopic signatures are more complicated (e.g., D4c, Figure 3c).

On the basis of this theoretical analysis, we have a closer inspection of the experimental data set of Figures 2 and 3 obtained by probing CUS of D1−D4 with CO adsorption, starting out again from D4 (Figure 3). Upon increasing the concentration of L4 (pydc$^{2−}$), the dominating CO bands located at ∼2179 cm^{-1} assigned to $Cu^{2+}−CO$ species (either parent or defective sites) become more and more asymmetrical, wider, and gradually red-shifted, before splitting into two bands at 2177 and 2169 cm^{-1}. Increasing the CO equilibrium pressure makes these changes more visible. Accordingly, the band at 2127 cm^{-1} with a shoulder band becomes wider and red-shifted. Subsequently, the shoulder evolves into a sharp peak at 2115 cm^{-1} superimposed by a new shoulder band at ∼2101

Figure 6. Thermal stability of CO adsorbed on defective sites by varying the concentration of defective linkers. UHV-FTIR spectra were obtained after CO (1×10^{-4} mbar) adsorption on the clean $[Cu_3(btc)_{2-d}(pydc)_d]$ (D4) at 90 K and then heating to the indicated temperatures. The concentration (d) of the defective linker L4 ($pydc^{2-}$) was varied: (a) $[Cu_3(btc)_{1.90}(L4)_{0.10}]$ (D4a); (b) $[Cu_3(btc)_{1.71}(L4)_{0.29}]$ (D4b); (c) $[Cu_3(btc)_{1.41}(L4)_{0.59}]$ (D4c).
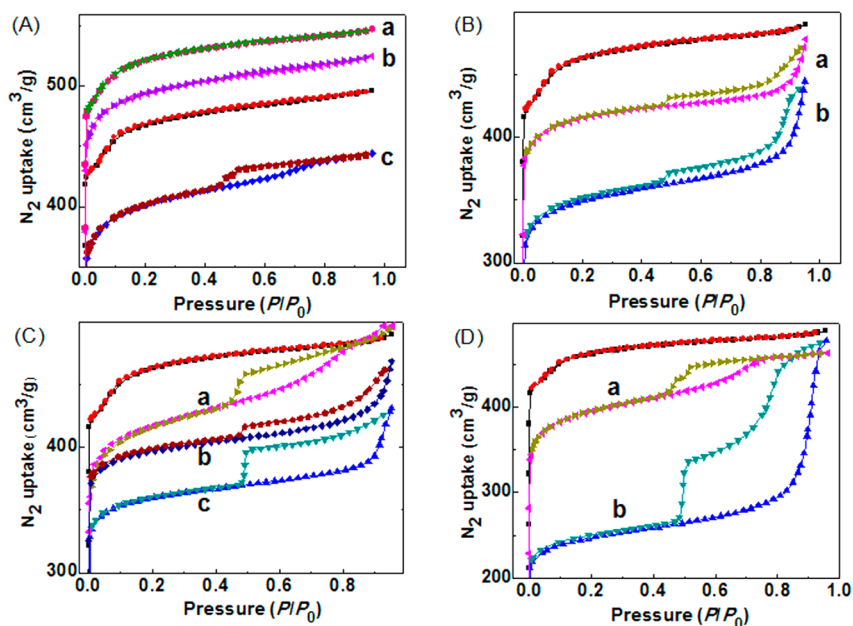
Figure 7. Experimental confirmation of the DMOF porosity. N_2 adsorption and desorption isotherms (78 K): (A) (a) $[Cu_3(btc)_{1.63}(L1)_{0.37}]$ (D1c); (b) $[Cu_3(btc)_{1.77}(L1)_{0.23}]$ (D1d); (c) $[Cu_3(btc)_{1.67}(L1)_{0.33}]$ (D1e); (B) (a) $[Cu_3(btc)_{1.59}(L2)_{0.41}]$ (D2b); (b) $[Cu_3(btc)_{1.63}(L2)_{0.37}]$ (D2d); (C) (a) $[Cu_3(btc)_{1.60}(L3)_{0.40}]$ (D3e); (b) $[Cu_3(btc)_{1.58}(L3)_{0.42}]$ (D3c); (c) $[Cu_3(btc)_{1.25}(L3)_{0.75}]$ (D3d); (D) (a) $[Cu_3(btc)_{1.71}(L4)_{0.29}]$ (D4b); (b) $[Cu_3(btc)_{1.41}(L4)_{0.59}]$ (D4c). The isotherms for the parent $[Cu_3btc_2]$ synthesized using $Cu(NO_3)_2$ are shown in black and reference isotherms are shown in red in (A)−(D). For clear display, the curves for D1c (A, a) and D1d (A, b) are vertically moved up by 30 and 50 cm^3 g^{-1}, while those of D2d (B, b) and D3d (C, c) are vertically moved down by 30 cm^3 g^{-1}. See the Supporting Information for pore size distributions.

cm^{-1}. High incorporated concentrations ($d > 20\%$) of L4 result in a quite complex pattern with red-shifted and superimposed bands (Figure 3c). These band evolutions upon stepwise increasing incorporation of L4 prove that the defect degree, i.e., mixed-valence Cu^{1+}/Cu^{2+} formation, can be precisely controlled by the choice of Lx and doping level d. Interestingly, D1−D3 exhibit similar but less drastic effects depending on the nature of L1−L3 and the applied doping level (Figure 2b−d). For example, the lowest intensity bands ranging from 2150 to 2157 cm^{-1} of D1−D4 (Figures 2 and 3), assigned to the weakly bound second CO−Cu^{1+} species, is indicative of the enhanced coordination space at the defect (Figure 4c; Figures S16 and S17, Supporting Information). Such a band is almost absent in D1e (Figure 2b), although it has a significant doping

concentration (16%). This observation is clearly related to the ligator properties of the nitro group with the largest steric bulk among Lx and closest similarity to the missing carboxylate ligator of btc^{3-}. Finally, notice the case of D3. The pronounced bands at 2125 and 2105 cm^{-1} assigned to Cu^{1+} (Figure 2d) illustrate that this system prefers copper reduction over deprotonation of the 5-hydroxy group for charge compensation in the course of L3 incorporation.

Temperature-dependent experiments of CO desorption on different DEMOFs (D1−D4) monitored by UHV-FTIRS can provide solid spectroscopic evidence for the binding strength of guest molecules at CUS, which is important for the catalytic behavior of materials (Figure 5, varying the defective linkers Lx; Figure 6, increasing the doping level d of L4). In all cases, with

increasing sample temperatures, the bands ranging from 2200 to 2160 cm^{-1} assigned to $(CO)Cu^{2+}$, and the bands at 2160−2150 cm^{-1} characteristic for one CO additionally binding to a $(CO)Cu^{1+}$ site, show a rapid decrease in intensity with relatively low binding energies (CO desorption at 100−130 K). The CO bands at lower frequencies (2150−2100 cm^{-1}) originating from $(CO)Cu^{1+}$ species are more stable and disappear only upon heating to 200−230 K, revealing that CO is more strongly bound to reduced Cu^{1+} CUS with a higher binding energy due to enhanced π back-donation. Notably, the stability of the $(CO)Cu^{2+}$ species in DEMOFs is comparable to or only slightly lower than that of $(CO)Cu^{2+}$ in the parent $[Cu_3btc_2]$.[41] These general features of the modified CUS of DEMOFs match very well with our QM/MM results of CO binding energies (Table S6, Supporting Information). Interestingly, D3e exhibits a very special behavior in that the band at 2157 cm^{-1} (assigned to the asymmetric stretch mode of $(CO)_2Cu^{1+}$) appears significantly more stable compared to those of all the other samples. A probable reason for this inconsistency is that CO molecules at the Cu^{1+} site may form a weakly stabilizing hydrogen bond with the proximal 5-hydroxy group of L3 (hydc^{2-}; see Scheme 1), which is not possible for the other Lx (Figure S10, Supporting Information). Sample D3e shows that DEMOFs with electronically modified CUS and simultaneously functionalized proximal coordination space can be derived. Such local tailoring of CUS may be very useful in multistep or cascade catalytic reactions.[52]

The derived atomistic model of diluted defects indicates control of the adsorbate stability at the modified CUS of DEMOFs. The stabilities of $(CO)Cu^{2+}$ for D4a−c tend to decrease with increasing doping level of L4 (Figure 6), illuminating that the introduced local defects may have effects on the whole framework. Notably, the corresponding behavior of the $(CO)_aCu^{1+}$ species ($a = 1, 2$) is particularly sensitive to Lx. Overall, these close inspections of the UHV-FTIR data show band evolutions and stability differences of CO adsorbed at Cu sites upon either doping the different kinds of Lx or increasing the degree of Lx incorporation, indicating that the particular effects on the relative abundance and stability of the specific $(CO)_aCu^{n+}$ species can be considered as a function of Lx and the doping level.

**3.3. N$_2$ Adsorption−Desorption Properties.** Standard N$_2$ adsorption−desorption experiments were carried out for D1−D4 with various Lx concentrations (Figure 7). The obtained isotherms confirm permanent porosity, framework rigidity, and different types of introduced mesopores. To gain a deeper understanding of these results, they should be correlated with the modification of CUS as discussed above. As qualitatively expected from the structure of L1 with a NO$_2$ ligator of steric bulk comparable to that of carboxylate (Scheme 1), the isotherms of D1c (Figure 7A, trace a) reveal no formation of mesopores. In contrast, linkers L2−L4 are more effective in modifying CUS locally and creating large-scale defects. Accordingly, D2b (Figure 7B, trace a) and D3c (Figure 7C, trace b) exhibit pronounced type H4 hysteresis loop isotherms.[53] D4b (Figure 7D, trace a) shows a type H2 hysteresis loop,[53] and D4c (Figure 7D, trace b) with further increased concentration of L4 exhibits an even more pronounced hysteresis loop with a stepwise desorption isotherm.[54] These findings reveal the formation of mesopores with different structures in D2−D4. The pore size distribution curves of both D3 and D4 determined by the Barret−Joyner−Halenda (BJH) method show the modulated and hierarchical

porosity upon varying the defective linkers and their framework-incorporated concentrations (Figure 7C,D).[54] All samples, except D4c, exhibit high values for the BET surface areas, being comparable to that of the parent $[Cu_3btc_2]$ (Table S5, Supporting Information).[55] The observation of a slight decrease of the BET surface area values for DEMOFs D1−D4 obtained by doping with defective linkers can be attributed to an increase of the pore sizes, resulting in the formation of mesopores.[38] It is well-known that the presence of mesopores is typically accompanied by certain loss of specific surface areas for the modified MOFs.[38,39,46,47,56,57] In addition, the corresponding IR and TGA data in the Supporting Information show that all the dominating features are characteristic for HKUST-1 frameworks, indicating no significant unreacted ligands remaining in their pores after being washed and activated. Therefore, we conclude that the hysteresis loops of isotherms observed for the DEMOFs result from mesopore formation with different pore structures. The origin of mesopore formation for all DEMOFs may be ascribed to the different types of local vacancies associated with the molecular structure and the different coordination modulation properties of the defective linkers Lx during the MOF synthesis.[38] The coordination chemistry of Lx (coordination bond equilibria) affects nucleation and crystal growth differently from that of the parent linker btc^{3-}.[58] Upon raising the concentration of the introduced Lx, the associated, slightly different kinds of coordination vacancies at the (defective) copper paddlewheel units may cluster. This effect eventually breaks the three types of neighboring pores of the parent structure (Figure S8, Supporting Information) and may connect them to each other to generate the observed large mesopores due to missing copper paddlewheels and/or linkages between them. However, the involved mechanisms are certainly very delicate as the isotherms of D1e and D3e exhibit type H2 hysteresis loops which are distinct from those of the corresponding reference samples synthesized from $Cu(NO_3)_2$ rather than $Cu(BF_4)_2$, while, notably, the parent $[Cu_3btc_2]$ derived from H$_3$btc with either of the two salts CuA$_2$ shows no mesopores at all. These observations illuminate template effects during synthesis, which are attributed to cooperative interactions between counteranions A (i.e., NO$_3$$^-$ and BF$_4$$^-$) of the employed CuA$_2$ and Lx. Consequently, the small-scale and large-scale defects are closely correlated and can be controlled by the choice of Lx, doping level d, and template anion A.

3.4. Evaluation of Reactive Properties. The parent $[Cu_3btc_2]$ is highly active for CO oxidation under clean UHV conditions at temperatures as low as 105 K.[41] Accordingly, the most defect-rich samples D4 were tested for CO oxidation under the same conditions (Figure S20, Supporting Information). The IR data revealed that high levels of mixed-valence Cu^{1+}/Cu^{2+} sites present in D4 exhibit special reactive properties due to the electronic modification at the CUS. The Cu^{2+} sites at Cu^{1+}/Cu^{2+} defects remain highly active for CO oxidation which occurs at 93 K, while CO is more strongly bound to the reduced Cu^{1+} CUS and does not react with O$_2$ to form CO$_2$ at low temperatures. Currently, we are investigating more complex reactions such as alcohol oxidation at DEMOFs. It was found that the parent $[Cu_3btc_2]$ is inactive for methanol oxidation, whereas this reaction occurs at the CUS of D4 due to the coexistence of Cu^{1+}/Cu^{2+}dimers and the functional defective linker L4 (pydc^{2-}). A detailed account of the high reactivity of DEMOFs for methanol oxidation will be published elsewhere. Furthermore, we have been studying the analogous

[Ru₃btc₂] case[59,60] and have discovered that the same kind of defect engineering modulates the electronic structure of the framework Ru sites very significantly. The obtained multifunctional DEMOFs (Ru) show quite unusual reactivity for CO_2 reduction in UHV at 90 K in the dark (Figure S21, Supporting Information) and are active catalysts for selective hydrogenation of olefins and for tandem reactions (cyclization/hydrogenation).

3.5. Optical and Magnetic Properties. The systematic defective linker doping offers fine-tuning of the DEMOFs' band gap. Figure 6a compares the diffuse reflectance spectra of perfect HKUST-1 with D1−D4. The reflection peaks of the DEMOFs exhibit a wider range and a stronger intensity. The band gap of as-synthesized (hydrated) parent HKUST-1 is determined to be about 2.87 eV, while the as-synthesized DEMOFs have larger band gaps ranging from 3.31 to 3.87 eV (Figure 8b). Accordingly, the visible color of the as-synthesized
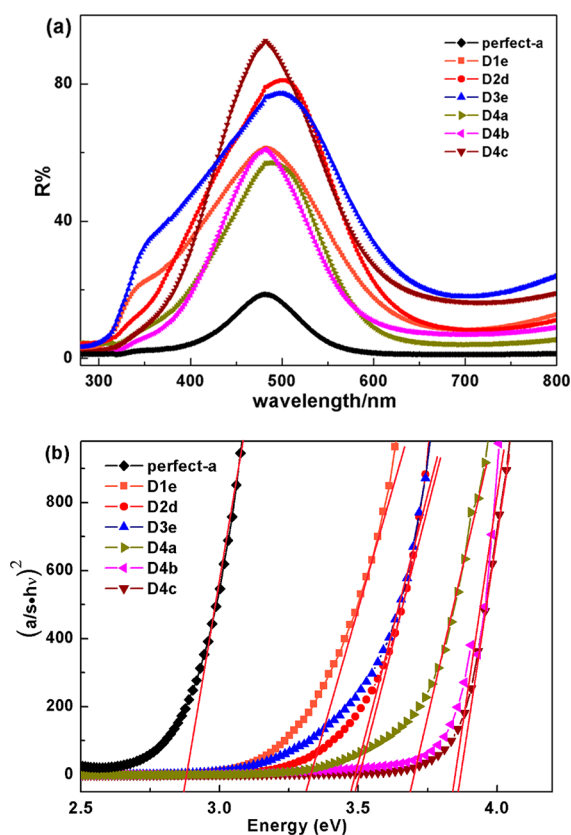

Figure 8. Diffuse reflectance spectrum (a) and band gap energy determination (b) of perfect HKUST-1 synthesized with $Cu(NO_3)_2$, namely, Perfect-a and D1−D4. The absorption spectra were calculated from reflectance spectra using the Kubelka−Munk function $a/S = (1 − R)^2/(2R)$, where a is the absorption coefficient, S is the scattering coefficient, and R is the reflectance, and are represented as a Tauc plot, $(a/S \cdot h\nu)^2$ vs $h\nu$. Evidently, the doping with Lx allows band gap engineering.

DEMOFs is paler than that of the parent material, showing that the Cu^{1+} sites are already present in the as-synthesized samples. From these data it is concluded that the Cu^{1+} species are predominantly formed during synthesis (ethanol as the reducing agent) and are not significantly generated by the activation protocol (heating under vacuum).

Accordingly, the magnetism of the mixed-valence DEMOFs responds to the degree of defective linker doping and the

corresponding modulation of the CUS. The data obtained for the parent HKUST-1 and D4b and D4c are discussed in the following. In general, all $\chi_M T$ vs T plots (Figure 9) show a
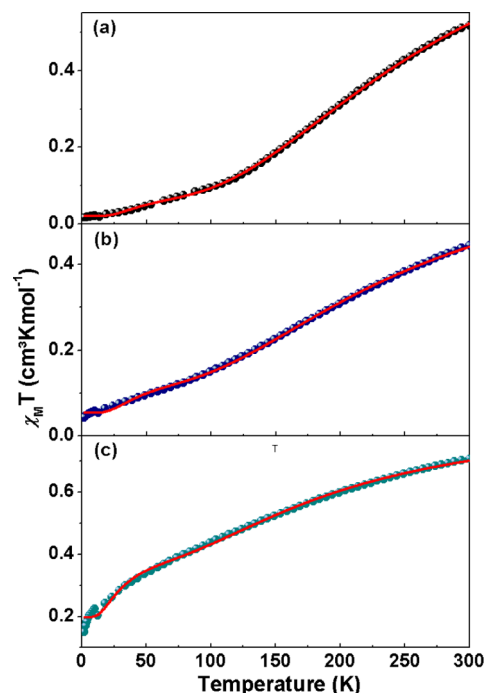
Figure 9. $\chi_M T$ vs T for (a) Perfect-a, i.e., the parent HKUST-1 MOFs synthesized with $Cu(NO_3)_2$, (b) $[Cu_3(btc)_{1.71}(L4)_{0.29}]$ (D4b), and (c) $[Cu_3(btc)_{1.41}(L4)_{0.59}]$ (D4c) (red solid lines represent the best theoretical fitting curves for plots of $\chi_M T$ vs T when $T > 80$ K).

continuous decrease upon cooling. This behavior is characteristic of antiferromagnetic exchange coupling for the parent paddlewheel units of Cu^{2+}, which are abundant within all the samples. Noticeably, the $\chi_M T$ vs T plots deviate from each other due to the different structural changes, affecting the electron spin resonance, magnetic coupling constant J of the Cu^{2+} dimers, and additional spin exchanges (ZJ') via btc$^{3−}$ and L4. The cw X-band EPR spectra at room temperature (Figure S9, Supporting Information) of all three samples show a broad signal with an isotropic g value of about 2.14 and different line widths ranging from 820 to 1060 G. This signal is typical for the $S = 1$ excited spin state of the antiferromagnetically coupled parent dimers of Cu^{2+} that are involved in additional spin exchange interactions via the aromatic framework.[61] The defective Cu^{1+}/Cu^{2+} dimers can be considered as monomeric, open-shell Cu^{2+} species (3d^9, $S = 1/2$, while closed-shell Cu^{1+} is diamagnetic, no coupling). Therefore, on the basis of the measured g values, the magnetic susceptibility data can be fitted using a refined model. It is based on the one described by O. Kahn for such samples containing Cu^{2+} paddlewheel units together with (diluted) monomeric Cu^{2+} species[62] and takes the additional spin exchange via btc$^{3−}$ and L4 (pydc$^{2−}$) into consideration. In the Supporting Information, the used model and fitting procedure are described in detail. The model fits well with $\chi_M T$ vs T plots for all the samples (Figure 9; the best fitting parameters and agreement factors R are listed in Table S7, Supporting Information). The increasing number of defects and fraction of diamagnetic impurities, assigned to Cu^{1+}, are reflected in the growing values of the fitting parameters ρ (uncoupled copper centers) and σ (copper centers coupled via

L4; see Table S7) and the lower g value compared to the experimental results. The sum of ρ and σ is larger than that deduced from the compositional data (elemental analysis and HPLC). The number of copper centers that do not couple over the μ-acetato bridge is not directly related to the number of Cu^{1+} ions in the sample. The J values of D4b and D4c of -330.2 ± 4.0 and -262.1 ± 9.3 cm^{-1}, respectively, are lower than that of the parent sample, -365.9 ± 1.7 cm^{-1} (which is comparable to previously reported data). The comparison of the J values indicates that the spin exchange interactions in the Cu^{2+} dimers decrease with increasing framework-incorporated concentration (d) of L4. For the parent sample, the value of spin exchange interactions via the aromatic framework (ZJ') is 70.1 ± 2.2 cm^{-1}, while those for D4b and D4c are -63.5 ± 2.7 and -41.8 ± 2.6 cm^{-1}, respectively. These characteristic differences are attributed to the different spin exchange interactions between the dimers, which are regulated by the doping linker as well as its framework-incorporated concentration and spatial distribution. These results further confirm the assumption of specific Cu^{1+} formation (already during synthesis, while not during activation and/or thermal treatment), which is controlled by the chosen doping linker Lx.

4. CONCLUSIONS

Our experimental results combined with theoretical calculations demonstrate consistently that MOFs can be surprisingly tolerant of systematic incorporation of defective linkers with broad functional variations of modified ligators to generate libraries of single-phased materials isoreticular to the parent structure. Defect engineering of MOFs will simultaneously modify the electronic properties and the proximate coordination space at reactive framework metal centers (i.e., CUS), as well as the pore structure of the MOF, eventually giving rise to functionalized mesopores in the case of stronger defect-generating properties and higher concentrations of implemented fragmented linkers. More recently, it has been reported that the introduction of "missing node" type defects into HKUST-1 by using isophtalic acid can finely tune the sorption properties of MOFs.[63] This multivariate nature of DEMOFs represents a new dimension for tailoring functions, which holds promise for moving beyond adsorption, separation, and catalysis by also targeting physical properties such as band gap engineering (Figure 8), magnetism (Figure 9), and eventually conductive properties.[64]

ASSOCIATED CONTENT

Ⓢ Supporting Information

Experimental details, characterization data obtained from EA, PXRD, TG, DSC, BET, pore size distributions, routine FTIR, UV−vis DRS, ^{1}H NMR, HPLC of quantitatively digested samples, and XPS, and the results of the calculations. This material is available free of charge via the Internet at http://pubs.acs.org.

AUTHOR INFORMATION

Corresponding Authors
wang@pc.rub.de
rochus.schmid@rub.de
roland.fischer@rub.de

Notes
The authors declare no competing financial interest.

REFERENCES

(1) Tuller, H. L.; Bishop, S. R. *Annu. Rev. Mater. Res.* **2011**, *41*, 369.
(2) Piao, Y. M.; Meany, B.; Powell, L. R.; Valley, N.; Kwon, H.; Schatz, G. C.; Wang, Y. H. *Nat. Chem.* **2013**, *5*, 840.
(3) Long, J. R.; Yaghi, O. M. *Chem. Soc. Rev.* **2009**, *38*, 1213.
(4) Horike, S.; Shimomura, S.; Kitagawa, S. *Nat. Chem.* **2009**, *1*, 695.
(5) Furukawa, H.; Cordova, K. E.; O'Keeffe, M.; Yaghi, O. M. *Science* **2013**, *341*, 974.
(6) So, M. C.; Jin, S.; Son, H. J.; Wiederrecht, G. P.; Farha, O. K.; Hupp, J. T. *J. Am. Chem. Soc.* **2013**, *135*, 15698.
(7) Carboni, M.; Abney, C. W.; Liu, S. B.; Lin, W. B. *Chem. Sci.* **2013**, *4*, 2396.
(8) Gallego, A.; Hermosa, C.; Castillo, O.; Berlanga, I.; Gomez-Garcia, C. J.; Mateo-Marti, E.; Martinez, J. I.; Flores, F.; Gomez-Navarro, C.; Gomez-Herrero, J.; Delgado, S.; Zamora, F. *Adv. Mater.* **2013**, *25*, 2141.
(9) Li, T.; Kozlowski, M. T.; Doud, E. A.; Blakely, M. N.; Rosi, N. L. *J. Am. Chem. Soc.* **2013**, *135*, 11688.
(10) Li, J.; Huang, P.; Wu, X. R.; Tao, J.; Huang, R. B.; Zheng, L. S. *Chem. Sci.* **2013**, *4*, 3232.
(11) Lee, J. Y.; Olson, D. H.; Pan, L.; Emge, T. J.; Li, J. *Adv. Funct. Mater.* **2007**, *17*, 1255.
(12) Yamada, T.; Otsubo, K.; Makiura, R.; Kitagawa, H. *Chem. Soc. Rev.* **2013**, *42*, 6655.
(13) Li, P. Z.; Maeda, Y.; Xu, Q. *Chem. Commun.* **2011**, *47*, 8436.
(14) Fischer, R. A.; Woll, C. *Angew. Chem., Int. Ed.* **2009**, *48*, 6205.
(15) Bradshaw, D.; Garai, A.; Huo, J. *Chem. Soc. Rev.* **2012**, *41*, 2344.
(16) Xiang, S. C.; Zhou, W.; Gallegos, J. M.; Liu, Y.; Chen, B. L. *J. Am. Chem. Soc.* **2009**, *131*, 12415.
(17) Bloch, E. D.; Queen, W. L.; Krishna, R.; Zadrozny, J. M.; Brown, C. M.; Long, J. R. *Science* **2012**, *335*, 1606.
(18) Dzubak, A. L.; Lin, L. C.; Kim, J.; Swisher, J. A.; Poloni, R.; Maximoff, S. N.; Smit, B.; Gagliardi, L. *Nat. Chem.* **2012**, *4*, 810.
(19) Bloch, E. D.; Murray, L. J.; Queen, W. L.; Chavan, S.; Maximoff, S. N.; Bigi, J. P.; Krishna, R.; Peterson, V. K.; Grandjean, F.; Long, G. J.; Smit, B.; Bordiga, S.; Brown, C. M.; Long, J. R. *J. Am. Chem. Soc.* **2011**, *133*, 14814.
(20) Liu, Y.; Kabbour, H.; Brown, C. M.; Neumann, D. A.; Ahn, C. C. *Langmuir* **2008**, *24*, 4772.
(21) Jeong, N. C.; Samanta, B.; Lee, C. Y.; Farha, O. K.; Hupp, J. T. *J. Am. Chem. Soc.* **2012**, *134*, 51.
(22) Hong, D. Y.; Hwang, Y. K.; Serre, C.; Ferey, G.; Chang, J. S. *Adv. Funct. Mater.* **2009**, *19*, 1537.
(23) Wu, H.; Zhou, W.; Yildirim, T. *J. Am. Chem. Soc.* **2009**, *131*, 4995.
(24) Hwang, Y. K.; Hong, D. Y.; Chang, J. S.; Jhung, S. H.; Seo, Y. K.; Kim, J.; Vimont, A.; Daturi, M.; Serre, C.; Ferey, G. *Angew. Chem., Int. Ed.* **2008**, *47*, 4144.
(25) Binnemans, K.; Lodewyckx, K. *Angew. Chem., Int. Ed.* **2001**, *40*, 242.
(26) Cairns, A. B.; Goodwin, A. L. *Chem. Soc. Rev.* **2013**, *42*, 4881.
(27) Kong, X. Q.; Deng, H. X.; Yan, F. Y.; Kim, J.; Swisher, J. A.; Smit, B.; Yaghi, O. M.; Reimer, J. A. *Science* **2013**, *341*, 882.
(28) Ameloot, R.; Vermoortele, F.; Hofkens, J.; De Schryver, F. C.; De Vos, D. E.; Roeffaers, M. B. J. *Angew. Chem., Int. Ed.* **2013**, *52*, 401.
(29) Chizallet, C.; Lazare, S.; Bazer-Bachi, D.; Bonnier, F.; Lecocq, V.; Soyer, E.; Quoineaud, A. A.; Bats, N. *J. Am. Chem. Soc.* **2010**, *132*, 12365.
(30) Xamena, F. X. L. I.; Cirujano, F. G.; Corma, A. *Microporous Mesoporous Mater.* **2012**, *157*, 112.
(31) Bunck, D. N.; Dichtel, W. R. *Chem.—Eur. J.* **2013**, *19*, 818.

(32) Park, T. H.; Hickman, A. J.; Koh, K.; Martin, S.; Wong-Foy, A. G.; Sanford, M. S.; Matzger, A. J. *J. Am. Chem. Soc.* **2011**, *133*, 20138.

(33) Marx, S.; Kleist, W.; Baiker, A. *J. Catal.* **2011**, *281*, 76.

(34) Vermoortele, F.; Bueken, B.; Le Bars, G.; Van de Voorde, B.; Vandichel, M.; Houthoofd, K.; Vimont, A.; Daturi, M.; Waroquier, M.; Van Speybroeck, V.; Kirschhock, C.; De Vos, D. E. *J. Am. Chem. Soc.* **2013**, *135*, 11465.

(35) Vermoortele, F.; Ameloot, R.; Alaerts, L.; Matthessen, R.; Carlier, B.; Fernandez, E. V. R.; Gascon, J.; Kapteijn, F.; De Vos, D. E. *J. Mater. Chem.* **2012**, *22*, 10313.

(36) Ravon, U.; Savonnet, M.; Aguado, S.; Domine, M. E.; Janneau, E.; Farrusseng, D. *Microporous Mesoporous Mater.* **2010**, *129*, 319.

(37) Wu, H.; Chua, Y. S.; Krungleviciute, V.; Tyagi, M.; Chen, P.; Yildirim, T.; Zhou, W. *J. Am. Chem. Soc.* **2013**, *135*, 10525.

(38) Park, J.; Wang, Z. Y. U.; Sun, L. B.; Chen, Y. P.; Zhou, H. C. *J. Am. Chem. Soc.* **2012**, *134*, 20110.

(39) Diring, S.; Furukawa, S.; Takashima, Y.; Tsuruoka, T.; Kitagawa, S. *Chem. Mater.* **2010**, *22*, 4531.

(40) Chui, S. S. Y.; Lo, S. M. F.; Charmant, J. P. H.; Orpen, A. G.; Williams, I. D. *Science* **1999**, *283*, 1148.

(41) Noei, H.; Amirjalayer, S.; Muller, M.; Zhang, X. N.; Schmid, R.; Muhler, M.; Fischer, R. A.; Wang, Y. M. *ChemCatChem* **2012**, *4*, 755.

(42) Wang, Y.; Glenz, A.; Muhler, M.; Woll, C. *Rev. Sci. Instrum.* **2009**, *80*, 113108.

(43) Xu, M. C.; Noei, H.; Fink, K.; Muhler, M.; Wang, Y. M.; Woll, C. *Angew. Chem., Int. Ed.* **2012**, *51*, 4731.

(44) Noei, H.; Gallino, F.; Jin, L. Y.; Zhao, J. L.; Di Valentin, C.; Wang, Y. M. *Angew. Chem., Int. Ed.* **2013**, *52*, 1977.

(45) Bureekaew, S.; Amirjalayer, S.; Tafipolsky, M.; Spickermann, C.; Roy, T. K.; Schmid, R. *Phys. Status Solidi B* **2013**, *250*, 1128.

(46) Qiu, L. G.; Xu, T.; Li, Z. Q.; Wang, W.; Wu, Y.; Jiang, X.; Tian, X. Y.; Zhang, L. D. *Angew. Chem., Int. Ed.* **2008**, *47*, 9487.

(47) Sun, L. B.; Li, J. R.; Park, J.; Zhou, H. C. *J. Am. Chem. Soc.* **2012**, *134*, 126.

(48) Hadjiivanov, K. I.; Vayssilov, G. N. *Adv. Catal.* **2002**, *47*, 307.

(49) Szanyi, J.; Daturi, M.; Clet, G.; Baer, D. R.; Peden, C. H. F. *Phys. Chem. Chem. Phys.* **2012**, *14*, 4383.

(50) St Petkov, P.; Vayssilov, G. N.; Liu, J. X.; Shekhah, O.; Wang, Y. M.; Woll, C.; Heine, T. *ChemPhysChem* **2012**, *13*, 2025.

(51) Prestipino, C.; Regli, L.; Vitillo, J. G.; Bonino, F.; Damin, A.; Lamberti, C.; Zecchina, A.; Solari, P. L.; Kongshaug, K. O.; Bordiga, S. *Chem. Mater.* **2006**, *18*, 1337.

(52) Luz, I.; Leon, A.; Boronat, M.; Xamena, F. X. L. I.; Corma, A. *Catal. Sci. Technol.* **2013**, *3*, 371.

(53) Sing, K. S. W. *Pure Appl. Chem.* **1985**, *57*, 603.

(54) Groen, J. C.; Peffer, L. A. A.; Pérez-Ramírez, J. *Microporous Mesoporous Mater.* **2003**, *60*, 1.

(55) Peralta, D.; Chaplais, G.; Simon-Masseron, A.; Barthelet, K.; Chizallet, C.; Quoineaud, A. A.; Pirngruber, G. D. *J. Am. Chem. Soc.* **2012**, *134*, 8115.

(56) Klimakow, M.; Klobes, P.; Rademann, K.; Emmerling, F. *Microporous Mesoporous Mater.* **2012**, *154*, 113.

(57) Du, H.; Bai, J.; Zuo, C.; Xin, Z.; Hu, J. *CrystEngComm* **2011**, *13*, 3314.

(58) Umemura, A.; Diring, S.; Furukawa, S.; Uehara, H.; Tsuruoka, T.; Kitagawa, S. *J. Am. Chem. Soc.* **2011**, *133*, 15506.

(59) Noei, H.; Kozachuk, O.; Amirjalayer, S.; Bureekaew, S.; Kauer, M.; Schmid, R.; Marler, B.; Muhler, M.; Fischer, R. A.; Wang, Y. M. *J. Phys. Chem. C* **2013**, *117*, 5658.

(60) Kozachuk, O.; Luz, I.; Xamena, F. X.; Noei, H.; Kauer, M.; Albada, H. B.; Bloch, E. D.; Marler, B.; Wang, Y.; Muhler, M.; Fischer, R. A. *Angew. Chem., Int. Ed.* **2014**, DOI: 10.1002/anie.201311128.

(61) Poppl, A.; Kunz, S.; Himsl, D.; Hartmann, M. *J. Phys. Chem. C* **2008**, *112*, 2678.

(62) Kahn, O. *Molecular Magnetism*; John Wiley & Sons Ltd.: Oxford, U.K., 1993.

(63) Barin, G.; Krungleviciute, V.; Gutov, O.; Hupp, J. T.; Yildirim, T.; Farha, O. K. *Inorg. Chem.* **2014**, DOI: 10.1021/ic500722n.

(64) Talin, A. A.; Centrone, A.; Ford, A. C.; Foster, M. E.; Stavila, V.; Haney, P.; Kinney, R. A.; Szalai, V.; El Gabaly, F.; Yoon, H. P.; Leonard, F.; Allendorf, M. D. *Science* **2014**, *343*, 66.